

# A Self-Assembly Method for Tunable and Scalable Nano-Stamps: A Versatile Approach for Imprinting Nanostructures

Yidenekachew J. Donie,\* Yingxuan Yuan, Isabel Allegro, Fabian Schackmar, Ihteaz M. Hossain, Robert Huber, Julie Roger, Ulrich W. Paetzold, Guillaume Gomard, and Uli Lemmer\*

In nanoimprint lithography (NIL), the imprinting stamp's fabrication is still a significant cost factor among the consumables. Bottom-up lithography approaches based on a phase-separation of polymer blends can provide a cost-effective route for fabricating these stamps. Today's polymers used to prepare phase-separated nanostructures (PSN), however, exhibit low glass transition temperatures. As a result, the PSN are prone to in-plane stamp distortions in the presence of high imprinting pressure and temperature, limiting their practical relevance for NIL. Here, the realization of mechanically and thermally stable PSN-based imprinting stamps for NIL systems via a phase-separation of a homopolymer/inorganic–organic hybrid polymer blend is reported. It is demonstrated that these imprinting stamps are easily tunable and scalable by adjusting the formulation of homopolymer/hybrid polymer mixture and deposition conditions. Feature sizes in PSN ranging from a few  $\mu\text{m}$  down to 100 nm are achieved through an interplay of these factors. As demonstrations of the envisioned applications, the developed imprinting stamps are integrated into a roll-to-roll NIL system for patterning a polystyrene thin-film. Moreover, light management is demonstrated by nanopatterning of a perovskite semiconductor in plate-to-plate process. The nanopatterned perovskite film achieves an integrated absorption and a photoluminescence emission peak increase of 7%<sub>rel</sub> and 121%<sub>rel</sub>, respectively.

## 1. Introduction

Nanoimprint lithography (NIL) is considered as an attractive solution for the fabrication of micro/nanostructures to enhance the performance of a wide variety of devices and materials, including flexible electronics (e.g., sensors,<sup>[1,2]</sup> solar cells,<sup>[2,3]</sup> and displays<sup>[4]</sup>), surface-enhanced Raman scattering substrates,<sup>[1,5]</sup> anti-counterfeiting labels,<sup>[6,7]</sup> antibacterial coatings,<sup>[8]</sup> and optical films.<sup>[9–12]</sup> The progress is driven by the need for micro/nanostructured materials with low-cost and high throughput on different surfaces, including flexible and curved ones.<sup>[13]</sup> In general, NIL utilizes a patterned stamp made of either hard or soft material (see Table S1, Supporting Information) for pattern transfer to the underlying film by mechanical deformation.<sup>[14]</sup> Hence, the imprinting stamp material is expected to exhibit relatively high hardness during the NIL process. Due to this requirement, silicon (Si) and quartz glass were the first and most widely used hard-imprinting stamp materials.<sup>[15,16]</sup> This is attributed to

the vast experience in patterning them using industrially established top-down nanopatterning techniques.<sup>[17]</sup> These materials, however, are more suitable for planar processing but not for roll-to-roll processing because of their limited mechanical flexibility. Their inflexibility, moreover, creates “air cavities” between the imprinting stamp and the underlying film in the presence of unwanted particles on the surface. This leads to a defect in the imprinted area as well as potential breakage of the stamp. Imprinting stamps made of soft and flexible materials, often polymer or polymer-ceramic based, have been developed to reduce the expensive hard material-based stamp strain. Furthermore, these stamp materials can reduce defects on an imprinted area due to unwanted particles by locally deforming around them.<sup>[18]</sup>

The imprinting stamp's fabrication is crucial and largely determines the NIL process's quality irrespective of the material used.<sup>[14,19]</sup> So far, imprinting stamps made of hard materials have been successfully fabricated by combining a variety of top-down lithographic approaches including, but

Y. J. Donie, Y. Yuan, I. Allegro, F. Schackmar, I. M. Hossain, R. Huber, J. Roger, U. W. Paetzold, G. Gomard, U. Lemmer  
Light Technology Institute

Karlsruhe Institute of Technology

Engesserstrasse 13, 76131 Karlsruhe, Germany

E-mail: yidenekachew.donie@kit.edu; ulrich.lemmer@kit.edu

F. Schackmar, I. M. Hossain, J. Roger, U. W. Paetzold, G. Gomard, U. Lemmer

Institute of Microstructure Technology

Karlsruhe Institute of Technology

Hermann-von-Helmholtz-Platz 1, 6344 Eggenstein-Leopoldshafen, Germany

 The ORCID identification number(s) for the author(s) of this article can be found under <https://doi.org/10.1002/admt.202101008>.

© 2021 The Authors. Advanced Materials Technologies published by Wiley-VCH GmbH. This is an open access article under the terms of the Creative Commons Attribution-NonCommercial-NoDerivs License, which permits use and distribution in any medium, provided the original work is properly cited, the use is non-commercial and no modifications or adaptations are made.

DOI: 10.1002/admt.202101008

not limited to, photo-,<sup>[20]</sup> e-beam-,<sup>[1]</sup> laser interference,<sup>[21]</sup> and colloidal lithography with dry/wet etching or electroplating.<sup>[22,23]</sup> In contrast, stamps made of soft materials such as polydimethylsiloxane (PDMS)<sup>[24]</sup> and ultraviolet (UV)-curable OrmoStamp<sup>[25]</sup> are commonly fabricated by combining the hard stamp fabrication techniques with soft NIL. To this end, the resulting stamps have been successfully used for patterning different functional materials (see Table S1, Supporting Information). Their fabrication, however, involves a complicated process and is usually time-consuming. In some cases, these processes are expensive to carry out and pose a challenge to further development of NIL-based devices (see Table S1, Supporting Information) in terms of commercialization. Bottom-up lithographic techniques, such as a self-assembly approach (SA) based on the phase-separation of polymer blends,<sup>[26]</sup> can offer a potential route to overcome this limitation. The attractiveness of SA for NIL-based devices (see Table S1, Supporting Information) results from its capacity to generate easily tunable quasi-periodic patterns to aperiodic, disordered ones with unique properties at high throughput and low-cost.<sup>[27–29]</sup> Its benefits are therefore well aligned with those provided by NIL. However, the conventional SA is commonly based on polymer materials that exhibit low glass transition temperatures.<sup>[26,30]</sup> Since a high temperature ( $\geq 100$  °C) is commonly required during the imprinting step, the thermal expansion coefficient plays an important role in the NIL process.<sup>[17,31]</sup> The lack of thermal stability of imprinting stamps causes in-plane stamp distortions or stress build-up during the cooling cycle.<sup>[17,31]</sup> Hence, it affects the pattern fidelity and registration accuracy. These issues have to be addressed to translate the SA benefits into a commercially viable NIL manufacturing process.

In this study, a UV-cross-linkable inorganic-organic hybrid polymer (OrmoStamp) is used as one of the two components of the polymer blend for the SA fabrication of the NIL stamp. Compared with the well-established polymers, for example, polystyrene (PS) and poly-methyl methacrylate (PMMA), used for phase-separated nanostructures (PSN) fabrication, OrmoStamp exhibits high thermal stability (up to 270 °C).<sup>[32]</sup> Furthermore, the values of OrmoStamp modulus of elasticity (650 MPa) and hardness (36 MPa) are sufficient for imprinting of micro-/nanostructures without in-plane stamp distortions.<sup>[32]</sup> These properties of OrmoStamp are attributed to its chemical composition, which contains Si-oxygen-Si networks connected covalently to the organic backbone.<sup>[32]</sup> OrmoStamp also demonstrates an excellent conformal contact and release (demolding) from imprinted patterns due to its low surface energy ( $23 \text{ mN m}^{-1}$ ).<sup>[16]</sup> The low surface energy is due to the fluorine additive of the Ormocere-based material and can also be modified by an anti-sticking layer depending on the choice of material to be imprinted and its substrate.<sup>[16]</sup> This property allows to produce multiple, identical working (OrmoStamp) stamps by replication from an OrmoStamp master stamp.<sup>[33]</sup> In addition, OrmoStamp has already gained significance for fundamental research and is already in use in industry as a successful imprinting stamp material in UV and thermal-based NIL.<sup>[25,32,34]</sup>

In what follows, we establish a stable and reproducible fabrication route for PSN (made of OrmoStamp) via SA on different substrates, including glass, silicon, flexible polymer, and

metal foils. Hence, it facilitates the straight forward integration of the PSN into different NIL systems as imprinting stamp independent of imprint contact types. The structural parameters (i.e., lateral size, thickness, density, and shape) of the PSN based imprinting stamps are tuned by adjusting the polymer blend deposition conditions and by tailoring the initial polymer mixture recipe (e.g., concentration, weight-ratio, and solvent). The versatility of the approach allows for specific tailoring of the PSN as required for the fabrication of light scattering layers in high-performance photonic devices. For example, the PSN-based imprinting stamps are integrated into plate-to-plate (P2P) NIL to pattern a metal halide perovskite layer and improve its light absorption capability for photovoltaic applications and light emission properties for light-emitting devices. Furthermore, we investigated the suitability of the PSN based imprinting stamps for roll-to-roll (R2R) NIL.

## 2. Results and Discussion

### 2.1. Formation of SA-Based Nano-Stamp

We formulated a single-phase solution consisting of a homopolymer—polystyrene (PS) and an inorganic-organic hybrid polymer—OrmoStamp for SA as illustrated in **Figure 1**. The single-phase solution is achieved by homogeneously dissolving the polymer blend in a common solvent (toluene). Then, the deposition of the solution using spin-coating on a substrate leads to PSN initiated by solvent removal from a homogeneous solution (see **Figure 1a,b**). After the formation of PSN, the OrmoStamp phase is solidified by UV-initiated crosslinking. This process leads to the formation of a 3D polymer network in OrmoStamp.<sup>[25,32]</sup> Thus, it makes the material resistant to oxygen ( $\text{O}_2$ ) plasma.<sup>[25,32]</sup> In contrast, the PS phase etching rate in  $\text{O}_2$  plasma (for details, refer to Experimental Section), that is,  $50 \text{ nm min}^{-1}$ , is unchanged by the UV-curing process. Consequently, an  $\text{O}_2$  plasma is used to etch the PS phase selectively and obtain PSN made of OrmoStamp. As an example, **Figure 1c,d** presents atomic force microscopy (AFM) images of the round-shaped PSN formed via nucleation and growth.<sup>[35,36]</sup> Before the selective etching of PS (see **Figure 1c**), the top surface morphology of the resulting PSN is composed of a continuous matrix with shallow nanoholes. The scale bar in the AFM image reveals an average nanohole depth of 40 nm. After  $\text{O}_2$  plasma treatment, nanopillars instead of the nanoholes were observed in the AFM image, as highlighted in **Figure 1d**. Based on the AFM images of the PSN before (**Figure 1c**) and after (**Figure 1d**) the  $\text{O}_2$  plasma treatment, it can be concluded that the polymer matrix is made of PS and the nanopillar domains of OrmoStamp. A cross-sectional scanning electron microscopy (SEM) image of a cut substrate, after  $\text{O}_2$  plasma etching of the PS matrix, has demonstrated the tendency of OrmoStamp to form a wetting layer, as highlighted in **Figure 1e**. This might be attributed to the difference in density ( $\rho$ ) between OrmoStamp ( $\rho = 1.14 \pm 0.01 \text{ g cm}^{-3}$ )<sup>[37]</sup> and PS ( $\rho = 0.97 \text{ g cm}^{-3}$ ).<sup>[38]</sup>

Previous studies have demonstrated that the nature of the common solvent (i.e., either selective or neutral to a polymer in the blend), which depends on the Hansen solubility

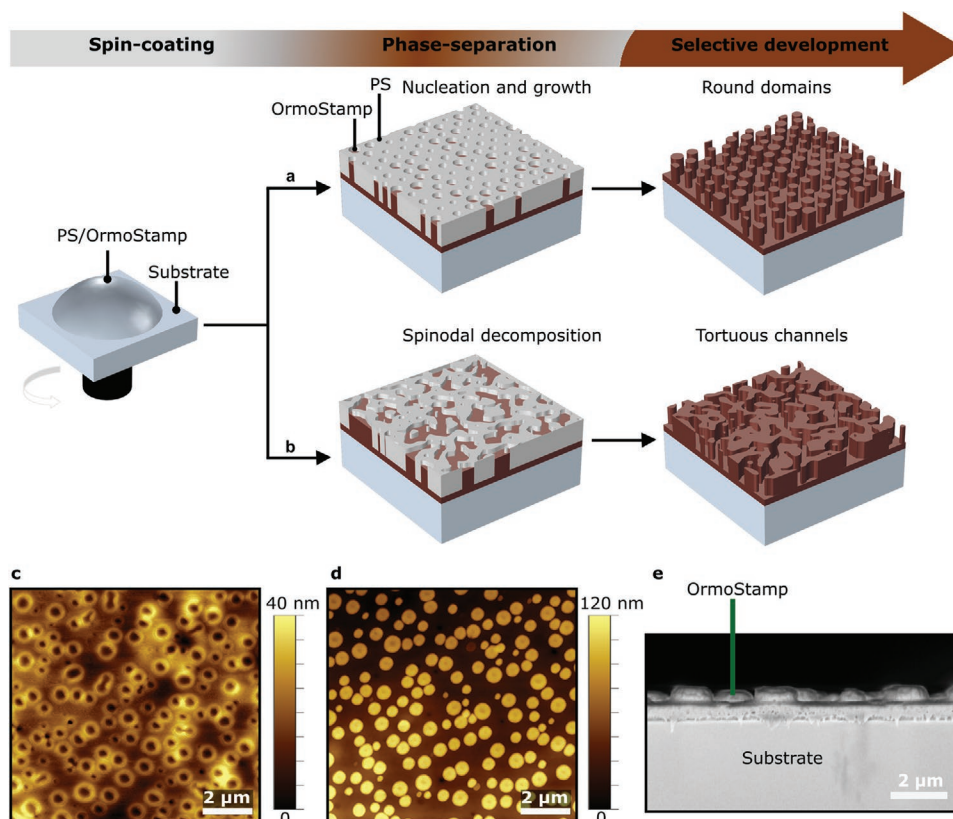


**Figure 1.** PS/OrmoStamp blend enables the direct patterning of OrmoStamp material via SA. A schematic illustration of the formation of spin-casted PSN via a) nucleation and growth, and b) spinodal decomposition mechanism at room temperature. Afterward, the PS matrix is selectively etched using  $O_2$  plasma treatment. AFM images of the PSN c) before and d) after  $O_2$  plasma treatment of a sample prepared using PS/OrmoStamp with a 3:1 ratio in the solvent toluene, with a concentration of  $35 \text{ mg mL}^{-1}$ . A spin-casting speed of 1500 rpm is used for producing the PSN. The OrmoStamp nanopillar top surface is represented by a black color in (c) and with a bright color in (d). e) Cross-sectional SEM image of the OrmoStamp nanopillars in (d).

parameters,<sup>[39]</sup> leads to different PSN morphologies.<sup>[40]</sup> This is because the polymer segment kinetic environment significantly depends on the solvent properties such as polarity and volatility.<sup>[41]</sup> Herein, particularly the shape of the PSN as illustrated in Figure 1a,b is tuned by the common solvent's mere choice. The PSN shown in Figure 1c,d are modified from round domains to a disordered bicontinuous network (tortuous channels) morphology by switching the blending solvent from toluene with relative polarity = 0.099<sup>[42]</sup> to higher polarity solvents (see Figure 2a,b). It is worth mentioning that similar

morphological changes are observed for the higher polarity solvents with lower (see Figure S1, Supporting Information) as well as higher (see Figure 2a,b) boiling points in comparison to toluene. The tortuous channel morphologies are formed via a spinodal decomposition mechanism. The formation of PSN by spinodal decomposition dominates when the homogeneous phase becomes thermodynamically unstable.<sup>[35,36]</sup> Outside of the spinodal decomposition region, that is, when the homogeneous phase becomes metastable, phase separation occurs via nucleation and growth.

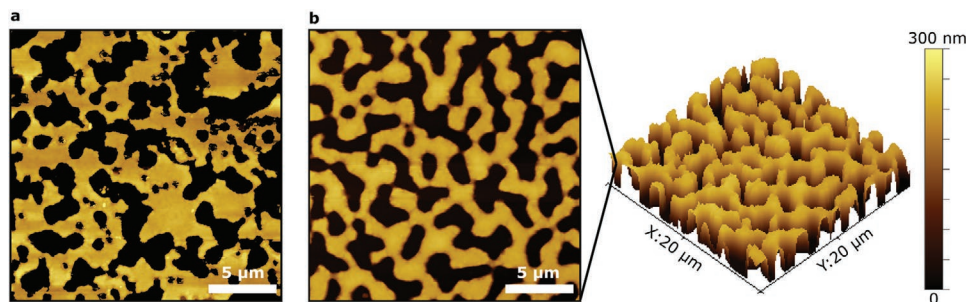


**Figure 2.** PS/OrmoStamp blend enables the formation of PSN with tunable shape. Tuning the shape of the PSN shown in Figure 1 by solely switching the common solvent from toluene to a) anisole and b) cyclohexanone. The 3D AFM image shows the PSN with wrinkle shapes fabricated with cyclohexanone.

The ability to easily fine-tune the structural parameters (e.g., height and lateral size, density, and inter-distance) of the imprinting stamps is high priority in NIL. In the following, we demonstrate the versatility of the developed imprinting stamps by tuning the PS/OrmoStamp deposition conditions and the initial mixture recipe.

## 2.2. Tuning the Morphology of SA-Based Imprinting Stamps

The morphology of the PSN can be controlled by adjusting the common solvent evaporation rate. This is attributed to the time-dependent domain coarsening behavior of PSN.<sup>[43,44]</sup> The spin-coating approach allows controlling the solvent evaporation rate and hence domain coarsening behavior of PSN by

simply adapting the rotational speed. Primarily, an increase in spin-casting speed shortens the time available for the OrmoStamp domains to coalesce into larger ones by accelerating the homogeneous solution's common solvent evaporation rate. Thus, it leads to the formation of finer OrmoStamp nanopillars at high speed. **Figure 3a** AFM images highlight the spin-casting speed's significant role in manipulating the PSN surface morphology. For example, PS/OrmoStamp solution spun at 500 rpm result in PSN with an average lateral size (LS) of 650 nm (film thickness = 160 nm), whereas the same solution spun at 3000 rpm result in PSN with LS = 290 nm (film thickness = 80 nm). A change in PSN surface morphology similar to that shown in Figure 3a can also be achieved by varying the PS/OrmoStamp concentration (refer to Figure 3b). In a spin-casted polymer solution, film thinning occurs through centrifugal and

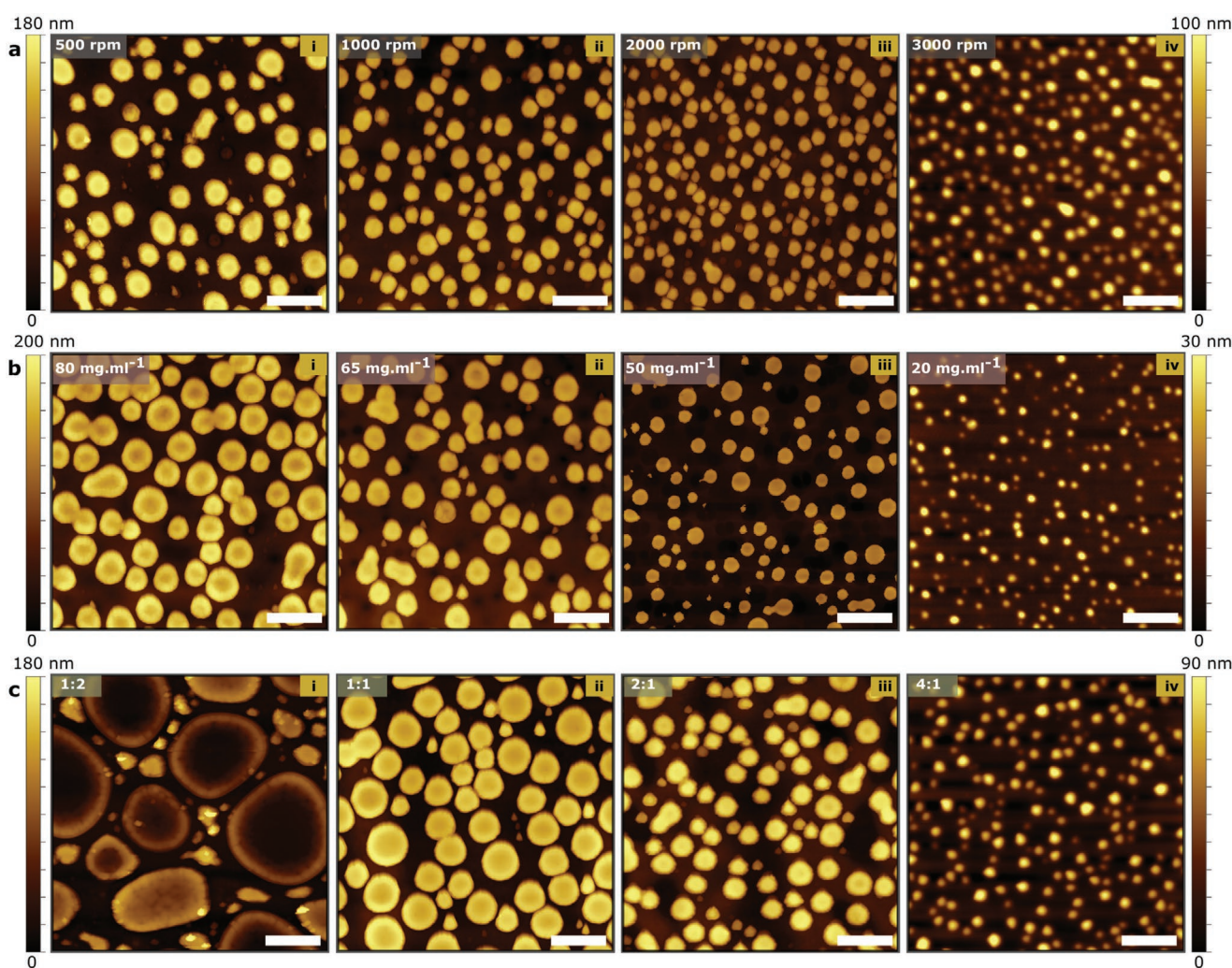


**Figure 3.** Influence of the ink composition and the deposition parameters on the resulting morphology of the PSN. a) AFM images of Ormostamp nanopillars fabricated using four different spin-casting speeds: i) 500, ii) 1000, iii) 2000, and iv) 3000 rpm. A PS/OrmoStamp = 3:1 blend in toluene solvent with a concentration of  $35 \text{ mg mL}^{-1}$  was used. b) AFM images of Ormostamp nanopillars prepared with different concentrations of PS/Ormostamp with a 3:1 weight ratio in toluene: i) 80, ii) 65, iii) 50, and iv)  $20 \text{ mg mL}^{-1}$ . A spin-casting speed of 1500 rpm is used to produce the PSN. c) AFM images of Ormostamp nanopillars prepared with different weight-ratios of PS and OrmoStamp in the blend, PS/OrmoStamp weight ratio: i) 1:2, ii) 1:1, iii) 2:1, and iv) 4:1. The blends were dissolved in toluene with a concentration of  $35 \text{ mg mL}^{-1}$  and spin-casted at 1500 rpm. All AFM images were acquired after the selective etching of the PS matrix using  $\text{O}_2$  plasma. The scale bar represents  $2 \mu\text{m}$  in all AFM images. The scale bar on the left and right sides of the AFM images represents the samples' height profiles in (i–iii) and (iv), respectively.

**Table 1.** Compilation of the structural parameters of the phase-separated OrmoStamp nanopillars fabricated with various spin-casting speeds, concentrations, and PS/OrmoStamp weight-ratios. For details of the data analysis, refer to Experimental Section.

| Parameter to tune                    | Value of parameter | Average height [nm] | LS [nm] | Filling fraction [%] | Effective period [nm] |
|--------------------------------------|--------------------|---------------------|---------|----------------------|-----------------------|
| Spin-speed (rpm)                     | 500                | 160                 | 650     | 29                   | 850                   |
|                                      | 1000               | 128                 | 539     | 30                   | 707                   |
|                                      | 1500               | 120                 | 460     | 31                   | 575                   |
|                                      | 2000               | 116                 | 433     | 33                   | 540                   |
|                                      | 3000               | 80                  | 290     | 20                   | 490                   |
| Concentration (mg mL <sup>-1</sup> ) | 80                 | 180                 | 890     | 53                   | 1100                  |
|                                      | 65                 | 156                 | 694     | 35                   | 690                   |
|                                      | 50                 | 138                 | 474     | 22                   | 710                   |
|                                      | 20                 | 24                  | 190     | 8                    | 720                   |
| Blend composition (PS/<br>OrmoStamp) | 1:1                | 172                 | 896     | 54                   | 900                   |
|                                      | 2:1                | 163                 | 632     | 34                   | 790                   |
|                                      | 4:1                | 74                  | 255     | 14                   | 890                   |

viscous forces.<sup>[45]</sup> The latter highly depends on the concentration of the polymer in the solution. A more diluted solution exhibits lower viscosity and higher diffusivity, leading to a thinner polymer film on the substrate. In contrast, undiluted solutions lead to a thicker layer, and such films are known to retain solvents for a more extended period. Thus, it provides sufficient time for the OrmoStamp nanopillar domains to coalesce into larger ones. As shown in Figure 3b, the LS of the PSN spun with a more dilute solution is significantly smaller (LS = 190 nm) as compared to that spun with the more concentrated solution (LS = 890 nm). Analogously, the in-plane structural parameters of the PSN can be adjusted by varying the weight ratio of the PS and OrmoStamp in the initial blend mixture. Since the high PS weight ratio (for a fixed PS/OrmoStamp solution concentration) also decreases the OrmoStamp concentration, it is expected that the PSN made of OrmoStamp resulting from a high PS weight ratio have smaller LS (refer to Figure 3c). When the OrmoStamp weight-ratio exceed 50%, a drastic change in the surface profile of the OrmoStamp morphology is observed. For OrmoStamp weight-ratio of 67%, one observes the formation of concave (sharp edges) topography as shown in Figure 3c(i) and Figure S2, Supporting Information. Such morphology is commonly observed when there is a small pressure difference across the surface skin of the phase-separated domains caused by a slow solvent evaporation, resulting in the collapse of top surface.<sup>[46]</sup> In contrast, when the OrmoStamp phase exceeds 75% in weight-ratio, an OrmoStamp matrix with nanoholes is observed instead of OrmoStamp nanopillars, as shown in Figure S3, Supporting Information. The change of the dispersed phase from OrmoStamp-rich to PS-rich, with change in blend composition, is known as phase-inversion.<sup>[47]</sup> The resulting phase-inversion phenomenon is commonly associated with the change in the viscosity ratio of the polymer blends.<sup>[47,48]</sup> It is predicted that the respective blend viscosity reaches a maximum at the point of phase inversion.<sup>[48]</sup>

Summing up the results above, the introduced nano-stamps fabrication route enables easy adaptation of the structural parameters of the nano-stamps by tailoring either the polymer

blend recipe or deposition conditions. However, independent control of the structural parameters of a nano-stamp by varying only one experimental parameter is challenging. For example, an increase in spin-casting speed not only leads to a decrease in the effective period (*P*) but also in the average height and lateral size as shown in Table 1. We also observed a trade-off between the different structural parameters of the nano-stamps for other experimental parameters as highlighted in Table 1. Therefore, it is essential to combine the different experimental parameters to achieve an optimal structural parameters of a nano-stamp for a given photonic application.

The application areas in which the developed PSN (made of OrmoStamp) can be applied are vast. The processes' adaptability allows for many technologies such as nano-transfer printing (i.e., transferring patterns between substrates by manipulating the adhesion forces between the nanophotonic OrmoStamp/functional material and the functional material/substrate), as illustrated in ref. [33]. In addition, the developed PSN can serve as antibacterial coatings<sup>[49]</sup> and light management nanostructures for optoelectronic devices.<sup>[28,50,51]</sup> In the following, we focus on using the PSN (made of OrmoStamp material) as an imprinting stamp to pattern different functional materials using NIL tools. Practically, these imprinting stamps can be directly integrated into the respective NIL systems regardless of the imprint contact types (i.e., P2P NIL,<sup>[52]</sup> roll-to-plate NIL,<sup>[53]</sup> and R2R NIL<sup>[1]</sup>). This is owing to the implemented fabrication approach, which allows the production of large-area imprinting stamps over a wide variety of substrates, including silicon wafers as large as 4 inches in diameter (Figure 4a), a semi-flexible polymer (Figure 4b), and a metal foil (Figure 4c). Similar PSN morphologies as highlighted in Figure S4, Supporting Information were obtained for samples prepared on various substrates (for a given PS/OrmoStamp blend and for the same spin-casting parameters). These manifold possibilities facilitate the development of imprinted photonic layers for various applications using different NIL systems. For example, the nano-stamps are integrated into R2R NIL system to pattern PS foils as discussed below.

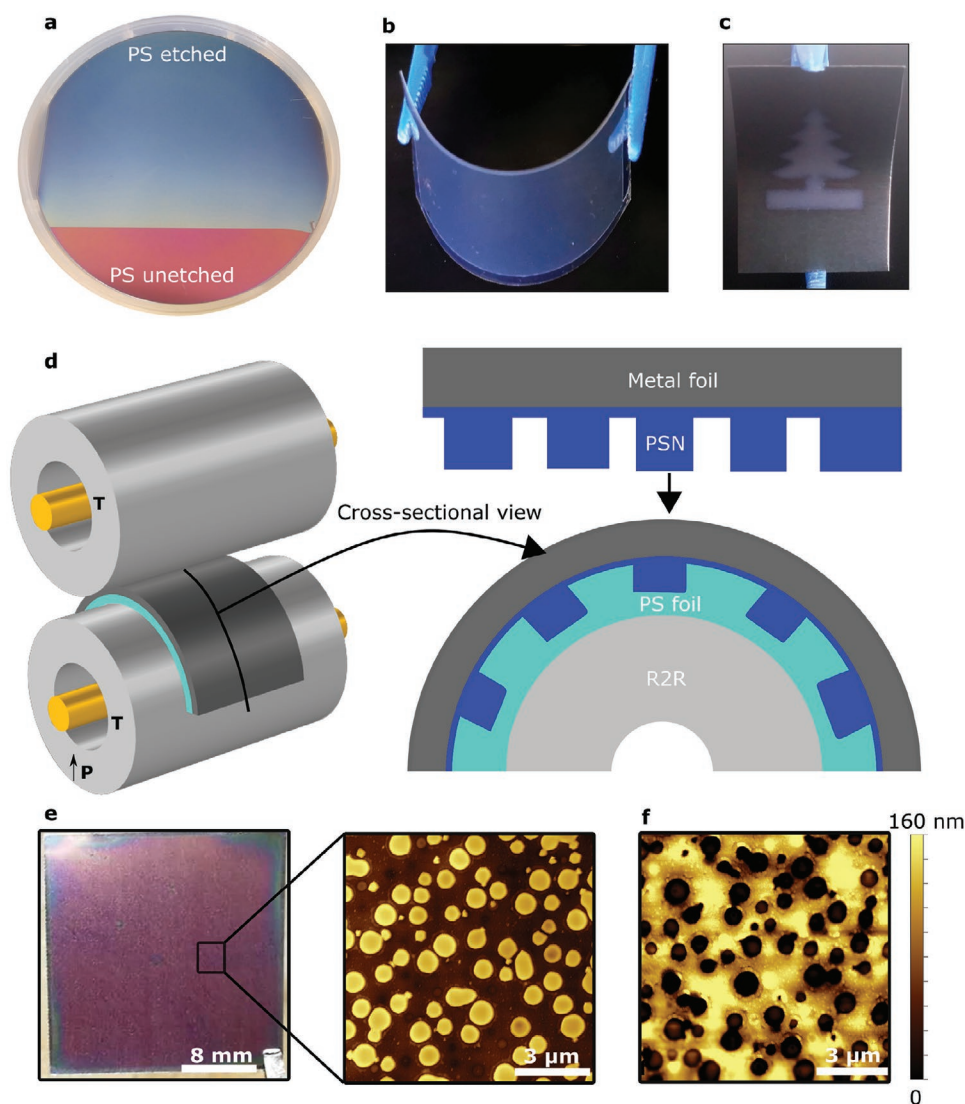


**Figure 4.** Versatility of the developed nano-stamps fabrication approach. Fabrication of nano-stamps on various substrates: a) Photograph of 4 inch silicon wafer coated with PS/OrmoStamp blend and after selectively etching of the PS matrix. The reddish area corresponds to the unetched part. b) Photograph of a flexible plastic foil (25 mm × 50 mm) made of polyethylene terephthalate and covered with OrmoStamp nanopillars after selective etching of the PS matrix. The blueish appearance is due to the optical scattering. c) Photograph of a Christmas tree logo on a flexible (stainless steel) metal foil (25 mm × 50 mm) formed by selectively etching the PS matrix in the foil's unmasked area. The samples in (a–c) were prepared using the same recipe as in Figure 1. A nano-stamp prepared using the metal foil substrate can be directly integrated into roll-to-roll hot embossing system to pattern PS foil. d) Schematic of the R2R hot embossing setup. The lower embossing cylinder carries the imprinting stamp and PS foil, both cylinders are heated, and pressure is applied to the lower cylinder. Controlled motors drive the upper and the lower embossing cylinder to realize a stable imprinting velocity. e) Photograph of the imprinting stamp based on PSN, fabricated on a stainless steel foil using PS/OrmoStamp = 3:1 with a concentration of 50 mg mL<sup>-1</sup>. The enlarged AFM image shows the corresponding surface morphology. f) AFM image of the nano-imprinted PS foil using an imprinting stamp shown in (e).

R2R systems can today produce imprinted thin film layers in the range of 0.2–30 m min<sup>-1</sup>, depending on the structures.<sup>[54,55]</sup> Nonetheless, R2R NIL holds much promise in enabling various new applications; their imprinting stamp fabrication is challenging. The challenge is the need for a cylindrical-shaped imprinting stamp. Based on the considerations above, the SA-based nanophotonic stamps are directly produced on a bendable metal foil to facilitate their integration into an in-house developed small-scale R2R embossing machine which is schematized in Figure 4d. Figure 4e displays the imprinting stamp

photograph obtained after selectively etching the PS phase using O<sub>2</sub> plasma. In an example process, the imprinting stamp was integrated into the R2R NIL system to pattern a 120 μm thick PS foil, as schematically shown in Figure 4d. Herein, the imprinting stamp is magnetically mounted onto an imprinting roller and used to imprint nanostructures under load into a PS foil. Complete height transfer from the imprinting stamp to the PS foil (Figure 4f) is achieved using an imprinting temperature close to the foil's glass transition (≈80 °C) and pneumatic cylinders pressure higher than 0.5 MPa. In addition, the

imprinted PS foil and the nano-stamp exhibit similar surface morphology as shown in the AFM images. This holds also true for the nanopatterns filling fraction and average lateral size of the imprinting stamp and the imprinted sample. The corresponding data are 32%, 31%, 621 nm and 614 nm, respectively. Details of the different imprinting parameters' effect on the PS film are discussed briefly in ref. [1]. Large-area imprinting stamps that comply with the industrial scale R2R fabrication process can be fabricated using scalable deposition methods for the PS/OrmoStamp blend instead of spin-coating. For example, complementary tests were carried out using doctor blading on metal foils (refer to Figure S5, Supporting Information) which resulted in the formation of PSN at room temperature. The finding highlights the up-scalability of the present approach and paves the way to numerous applications that require the direct fabrication of functional nanostructures on flexible substrates using R2R processing. By tuning the polymer blend ink formulation, the PSN-based imprinting stamps may also be prepared using inkjet printing.<sup>[29,56]</sup> This approach allows the PSN to be rapidly processed into the desired macroscopic design.<sup>[29]</sup>

Moreover, the developed nano-stamps that feature structural disorder are very attractive to design efficient light management patterns for large area optoelectronic devices where a cost effective method for patterning is needed.<sup>[27,57–59]</sup> The two highly relevant applications are solar cells and displays. Thus, the developed nano-stamps are explored in the following section to fabricate nanostructured metal halide perovskite layers for photovoltaic and light-emitting device applications using P2P NIL tool.

### 2.3. PSN Enabled Nanophotonic Perovskite Layer for Optoelectronic Devices

For the last few years, metal halide perovskite semiconductors have attracted a lot of attention in optoelectronic device research as they offer strong optical absorption and emission, as well as high charge carrier mobilities.<sup>[52,60–63]</sup> Furthermore, the attractiveness of NIL for perovskite-based devices results from the fact that these semiconductors are low-cost materials and can be processed with a wide range of cost-effective fabrication approaches, including roll-to-roll processing.<sup>[64]</sup> Compared to unpatterned perovskite thin films, the nano-imprinted ones exhibit intriguing and unusual optical properties in various photonic devices and materials such as solar cells,<sup>[52]</sup> light-emitting diodes,<sup>[61]</sup> lasers,<sup>[63]</sup> metamaterials,<sup>[60]</sup> and photodetectors.<sup>[62]</sup> In this direction, direct patterning of perovskite thin films using thermal NIL has attracted much attention as it does not involve gases or solvents for patterning. The approach is mainly based on planar perovskite film recrystallization under pressure and heat in the presence of an imprinting stamp.<sup>[52]</sup> The exclusion of gases or solvents in the patterning process is essential since most perovskites are soluble materials.

In the following, we demonstrate the SA-based imprinting stamp's suitability for patterning perovskite material using the thermal P2P NIL method and thereby improving its light absorption capability. As a proof-of-concept, the PSN made of nano-stamps shown in Figures 1d and 3a(iii,iv) are

used as imprinting stamps. Before their integration into the thermal NIL tool, the imprinting stamps were treated with 1H,1H,2H,2H-perfluorooctyltrichlorosilan to improve their anti-sticking property and to reduce the demolding forces substantially.<sup>[16]</sup> Afterward, the thermal NIL of the triple cation perovskite ( $\text{Cs}_{0.1}(\text{MA}_{0.17}\text{FA}_{0.83})_{0.9}\text{Pb}(\text{I}_{0.83}\text{Br}_{0.17})_3$ ) films was conducted with a temperature of  $\approx 100$  °C and a pressure of  $\approx 60$  MPa in a nitrogen environment, as illustrated schematically in Figure 5a. The surface morphology of the nano-imprinted perovskite films and planar can be seen in the AFM images in Figure 5b–d and Figure S6, Supporting Information, respectively. Figure 5b also includes the photograph of the nano-imprinted perovskite film. The nanoholes of the nano-imprinted perovskite films show an average depth of 80 nm.

Figure 5e highlights the absorption increase following the integration of the PSN using thermal NIL into the perovskite material and the enhanced harvesting of low-energy photons with respect to unpatterned perovskite material. As revealed by AFM images, this can notably attributed to the regular nanohole pattern imprinted into the perovskite material. This results in an enhanced light-scattering and an efficient light coupling into the film. The overall spectrally weighted absorptance, integrated absorption (IA), was calculated to assess the different perovskite films' light-harvesting capabilities under consideration. In the case of the unpatterned ("planar") perovskite films, the IA is 62.3%. On the other hand, the patterned perovskite films based on the PSN with  $P = 490, 540,$  and  $575$  nm improve the IA by 7, 4.6, and 4% relative to the planar counterpart, respectively. Herein, highest optical absorption gain is observed for the pattern with the smallest  $P$ . A strong optical absorption enhancement was also observed by Schmager et al. for periodically patterned perovskite films using optical simulation when the period of the pattern is  $P = 300\text{--}500$  nm compared to other  $P$  values.<sup>[65]</sup> Figure 5f shows enhanced photoluminescence (PL) spectra from the three nano-imprinted perovskite films compared to a planar counterpart. Quantitatively, the PL emission peak (located near the band-gap of the perovskite material) is enhanced by 47, 48, and 121%<sub>rel</sub>, respectively. As such, our approach offers promising avenues for improving perovskite light-emitting diodes efficiency by enabling high photon emission due to favored nanostructure morphology, contributing to better light out-coupling compared to pristine ones. Emission enhancement above the bandgap of the perovskite is suppressed due to the dominate absorption.

## 3. Conclusion

SA based on the phase-separation of polymer blends offer a versatile platform for fabricating easily tunable quasi-periodic patterns for nanophotonics applications. This study demonstrated a stable and reproducible fabrication route for PSN based imprinting stamps with tunable structural parameters for NIL using SA. Herein, a completely new ink-formulation consisting of the homopolymer—PS and the inorganic-organic hybrid polymer—OrmoStamp is established to meet the demanding process requirements. The phase-separated OrmoStamp domains tuned from a few  $\mu\text{m}$  down to 100 nm range. The PSN structural parameters were tuned over

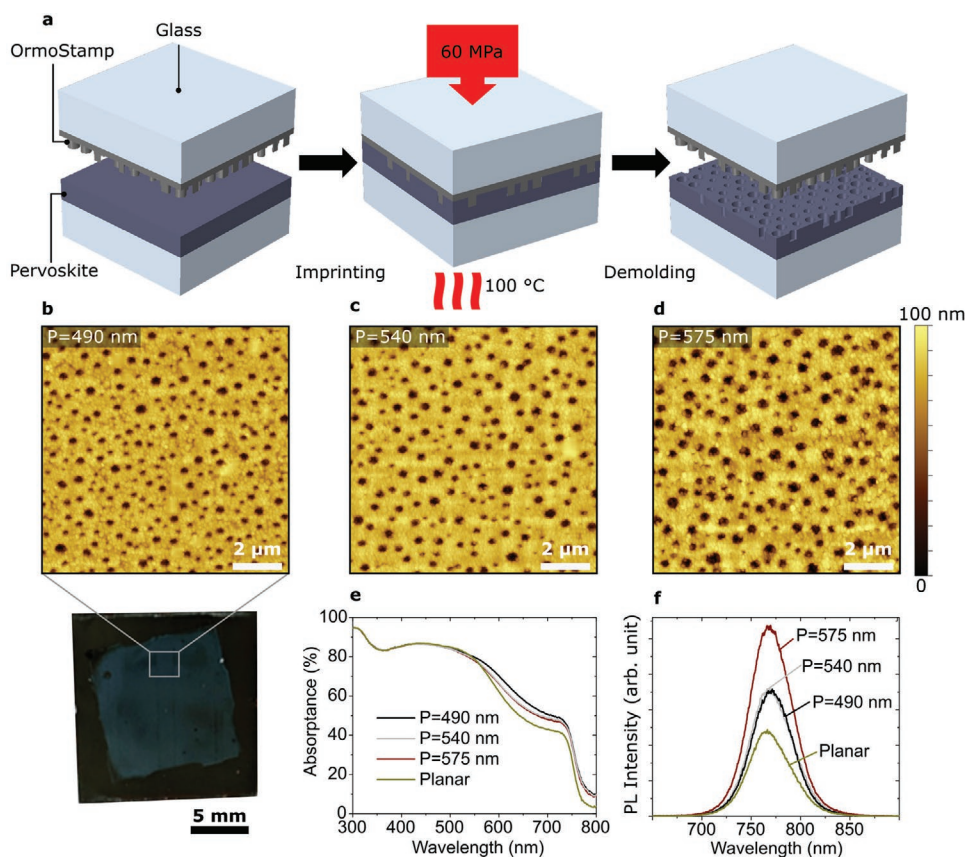


**Figure 5.** Improved light management in nano-imprinted perovskite films using PSN based imprinting stamp. a) Schematic illustration of the imprinting process of the perovskite films on glass using P2P NIL tool. Imprinting stamps with surface relief shown in Figures 1d and 3a(iii,iv) are used for the thermal NIL process. The calculated  $P$  of the nano-stamps are shown in Table 1. b–d) AFM images of the corresponding nano-imprinted perovskite films with effective period of b)  $P = 490$  nm, c)  $P = 540$  nm, and d)  $P = 575$  nm. The photograph of the imprinted perovskite film using  $P = 490$  nm is shown in (e). e) Optical absorption of the planar and the patterned perovskite films with a thickness of 250 nm. f) PL spectrum of the planar perovskite film compared to the PL spectrum of three different nano-imprinted films.

various substrates through an interplay of the initial polymer blend recipe and process parameter. The resulting PSN based on OrmoStamp, owing to the material's nature, exhibit excellent bulk flexibility with mechanical stability. We have shown that PSN made of OrmoStamp can serve as an imprinting stamp for patterning perovskite films via thermal P2P NIL and thereby significantly improving its optical absorption and emission with respect to its planar counterpart. Our findings reveal an easy way to produce imprinting stamps valid for thermal NIL and promising for UV-based NIL. We have also devised the PSN on a flexible metal foil and integrated it into R2R NIL to nano-pattern a polystyrene film. As this cost-effective method can be readily scaled up to large areas, we anticipate that it will foster the widespread implementation of PSN in NIL-based nanophotonic devices.

#### 4. Experimental Section

**Fabrication of Imprinting Stamps by a Self-Assembly Method:** PS (molecular weight = 100 kg mol<sup>-1</sup>) and OrmoStamp were purchased from Alfa Aesar Johnson Matthey and micro resist technology GmbH, respectively. PS/OrmoStamp mixtures with different mass ratios and concentrations were prepared and dissolved in toluene (Alfa Aesar

99.8%), cyclohexanone (Alfa Aesar 99%), and anisole (Sigma Aldrich 99.7%). A PS/OrmoStamp film was prepared by spin-coating the blend mixtures onto different substrates. Before deposition, the substrates based on glass (Schott), silicon (Siegest wafer GmbH), metal foil (Record metall-folien GmbH), and polyethylene terephthalate (Putz GmbH + Co. Folien KG) were cleaned in acetone and isopropanol in an ultrasonic bath for 10 min each, dried with nitrogen. After the phase separation of the polymer blends, PS was selectively etched using oxygen plasma (Femto, Diener electronics GmbH + Co. KG) at an operational power of 100 W, and the O<sub>2</sub> flow rate was fixed at 45 cm<sup>-3</sup> min (qn). Unless mentioned otherwise, relative humidity was maintained between 40% and 50% during spin coating.

**Fabrication of Perovskite Layer:** Plain glasses (Schott) were used as substrates. The substrates were cleaned in acetone and isopropanol in an ultrasonic bath for 10 min each, and then dried with nitrogen and exposed to oxygen plasma (Femto, Diener electronics GmbH + Co. KG) for 3 min. The triple cation perovskite solution (Cs<sub>0.1</sub>(MA<sub>0.17</sub>FA<sub>0.83</sub>)<sub>0.9</sub>Pb(I<sub>0.83</sub>Br<sub>0.17</sub>)<sub>3</sub>) was prepared with the precursors of methylammonium bromide (MABr, Dyesol), formamidinium iodide (FAI, Dyesol), lead iodide (PbI<sub>2</sub>, TCI), lead bromide (PbBr<sub>2</sub>, TCI), and cesium iodide (CsI, Alfa Aesar). The precursor solution for the perovskite film was prepared by mixing FAI (0.5 M), PbI<sub>2</sub> (0.55 M), MABr (0.1 M), and PbBr<sub>2</sub> (0.1 M) in DMF:DMSO (ratio 4:1). CsI in DMSO (1.5 M) was then added to form Cs<sub>0.1</sub>(MA<sub>0.17</sub>FA<sub>0.83</sub>)<sub>0.9</sub>Pb(I<sub>0.83</sub>Br<sub>0.17</sub>)<sub>3</sub>. The perovskite films were prepared using spin-coating method (as described in ref. [52,66]). Before thermal NIL (see below), the samples were annealed at 100 °C for 1 h in a nitrogen atmosphere.

**Thermal Nanoimprint Lithography:** For the embossing of the self-assembled nanostructures into the perovskite layers, a custom-made vacuum-based P2P hot embossing machine developed in cooperation with Jenoptik Mikrotechnik was implemented.<sup>[67]</sup> Herein, the imprinting stamp and substrate coated with perovskite layer were stacked and placed between the upper and lower plates of the P2P hot embossing machine. In an initial step the chamber was evacuated and vented with nitrogen. Then, the two plates applied a contact force of 1 MPa between stamp and sample. The temperature was increased up to 100 °C and upon reaching the desired temperature (after ≈8 min) a force of 60 MPa was applied for 5 min while the temperature was kept constant. In the next step, the temperature was cooled down to 40 °C and upon reaching this temperature (after ≈ 8 min) the pressure was released. The lower and upper plates were heated and cooled via an oil heating and cooling unit.

**Topographical Investigation:** The thickness measurements of the perovskite films were performed using a profilometer (Bruker Dektak XT). The imprinted perovskite films' morphology and self-assembled nanostructures were investigated by using a JPK nanoWizard II atomic force microscope in intermittent contact mode under ambient conditions. The cross-section view image was acquired using scanning electron microscopy (SUPRA 60VP, Carl Zeiss Microscopy GmbH); the sample was cut and coated with a thin gold layer using JFC-1200 fine coater (JEOL) beforehand.

**Optical Characterization:** Optical characteristics of the perovskite films were extracted out of transmittance (*T*) and reflectance (*R*) data, which were measured using a UV-vis spectrometer (Lambda 1050, PerkinElmer Inc.) equipped with a 150 mm integrating sphere. The perovskite film characterization was carried out in an ambient atmosphere. The absorbance (*A*) of the samples was then derived by applying  $A = 1 - T - R$  for every wavelength. PL measurements were performed using an in-house PL setup in an ambient atmosphere. PL emission profile was measured using a spectrometer (Acton SpectraPro SP-2300) pointing toward the sample, which was mounted on an adjustable stage. The perovskite films were excited using a pulsed Picolo-10 laser from InnoLas Laser GmbH (532 nm, repetition rate: 1 kHz, pulse width: 800 ps).

**Statistical Analysis:** The data presented in Table 1 as single variables to quantify the self-assembled nanostructures were calculated by applying different image processing software's on the measured AFM images. For example, the pair correlation function (radial distribution) discussed in ref. [68] was used to derive the nanopillars effective period (which is the nearest neighbor peak of the function). The average lateral scale and filling fraction of the self-assembled nanopillars were calculated using ImageJ software.<sup>[69]</sup> The height distribution of the self-assembled nanopillars was investigated using Gwyddion software.<sup>[70]</sup>

## Supporting Information

Supporting Information is available from the Wiley Online Library or from the author.

## Acknowledgements

The authors thank R. Schmagel for fruitful discussions. Y.J.D. is part of the Max Planck School of Photonics supported by BMBF, Max Planck Society, and Fraunhofer Society. The authors gratefully acknowledge support from the Karlsruhe Nano Micro Facility for Information-driven Material Structuring and Characterization (KNMFi) and Karlsruhe School of Optics & Photonics (KSOP). This research has also been funded by the Deutsche Forschungsgemeinschaft (DFG, German Research Foundation) under Germany's Excellence Strategy via the Excellence Cluster 3D Matter Made to Order (EXC-2082/1-390761711) and through the DFG priority program SPP 1839 "Tailored disorder."

Open access funding enabled and organized by Projekt DEAL.

## Conflict of Interest

The authors declare no conflict of interest.

## Data Availability Statement

Research data are not shared.

## Keywords

light management, nanoimprint lithography, nanophotonic stamp, perovskite, self-assembly

Received: September 6, 2021

Revised: October 23, 2021

Published online:

- [1] A. Habermehl, P. Brenner, R. Huber, A. Mertens, F. Winkler, L. Hahn, M. Guttman, C. Eschenbaum, U. Lemmer, *Adv. Eng. Mater.* **2019**, *21*, 1900110.
- [2] J. Shao, X. Chen, X. Li, H. Tian, C. Wang, B. Lu, *Sci. China Technol. Sci.* **2019**, *62*, 175.
- [3] M. Soldera, Q. Wang, F. Soldera, V. Lang, A. Abate, A. F. Lasagni, *Adv. Eng. Mater.* **2020**, *22*, 1901217.
- [4] R.-P. Xu, Y.-Q. Li, J.-X. Tang, *J. Mater. Chem. C* **2016**, *4*, 9116.
- [5] C. Zhang, P. Yi, L. Peng, X. Lai, J. Chen, M. Huang, J. Ni, *Sci. Rep.* **2017**, *7*, 39814.
- [6] K. G. Lee, B. G. Choi, B. I. Kim, T. Shyu, M. S. Oh, S. G. Im, S.-J. Chang, T. J. Lee, N. A. Kotov, S. J. Lee, *Adv. Mater.* **2014**, *26*, 6119.
- [7] A. Colniță, D. Marconi, I. Brezeștean, R.-D. Pașca, I. Kacso, L. Barbu-Tudoran, I. Turcu, *Anal. Lett.* **2021**, *54*, 302.
- [8] F. Dundar Arisoy, K. W. Kolewe, B. Homyak, I. S. Kurtz, J. D. Schiffrman, J. J. Watkins, *ACS Appl. Mater. Interfaces* **2018**, *10*, 20055.
- [9] A. Roslizar, S. Dottermusch, R. Schmagel, M. Guttman, G. Gomard, H. Hölscher, B. S. Richards, U. W. Paetzold, *Sol. Energy Mater. Sol. Cells* **2020**, *214*, 110582.
- [10] B. Dong, N. Lu, M. Zelsmann, N. Kehagias, H. Fuchs, C. M. Sotomayor Torres, L. Chi, *Adv. Funct. Mater.* **2006**, *16*, 1937.
- [11] J. Song, H. Lu, K. Foreman, S. Li, L. Tan, S. Adenwalla, A. Gruverman, S. Ducharme, *J. Mater. Chem. C* **2016**, *4*, 5914.
- [12] B. Radha, S. H. Lim, M. S. Saifullah, G. U. Kulkarni, *Sci. Rep.* **2013**, *3*, 1078.
- [13] Z. Li, Y. Gu, L. Wang, H. Ge, W. Wu, Q. Xia, C. Yuan, Y. Chen, B. Cui, R. S. Williams, *Nano Lett.* **2009**, *9*, 2306.
- [14] N. Kooy, K. Mohamed, L. T. Pin, O. S. Guan, *Nanoscale Res. Lett.* **2014**, *9*, 320.
- [15] J. Rodríguez-Hernández, A. L. Cortajarena, *Design of Polymeric Platforms for Selective Biorecognition*, Springer, Berlin, Heidelberg **2015**.
- [16] M. Papenheim, C. Steinberg, K. Dhima, S. Wang, H.-C. Scheer, *J. Vac. Sci. Technol., B: Nanotechnol. Microelectron.: Mater., Process., Meas., Phenom.* **2015**, *33*, 06F601.
- [17] L. J. Guo, *Adv. Mater.* **2007**, *19*, 495.
- [18] B. Kwon, J. H. Kim, *J. Nanosci.* **2016**, 2016.
- [19] P. Ma, Z. Xu, M. Wang, L. Lu, M. Yin, X. Chen, D. Li, W. Ren, *Mater. Res. Bull.* **2017**, *90*, 253.
- [20] D. Wagner, A. Jayatissa, in *Nanofabrication: Technologies, Devices, and Applications II*, vol. 6002, SPIE, Bellingham, WA **2005**.
- [21] A. P. Amalathas, M. M. Alkai, J. Thirumalai, in *Micro/Nanolithography: A Heuristic Aspect on the Enduring Technology*, IntechOpen, London **2018**.

- [22] C.-W. Kuo, J.-Y. Shiu, Y.-H. Cho, P. Chen, *Adv. Mater.* **2003**, *15*, 1065.
- [23] B. Wang, W. Zhao, A. Chen, S.-J. Chua, *J. Cryst. Growth* **2006**, *288*, 200.
- [24] U. Plachetka, M. Bender, A. Fuchs, B. Vratzov, T. Glinsner, F. Lindner, H. Kurz, *Microelectron. Eng.* **2004**, *73*, 167.
- [25] M. Mühlberger, I. Bergmair, A. Klukowska, A. Kolander, H. Leichtfried, E. Platzgummer, H. Loeschner, C. Ebm, G. Grützner, R. Schöftner, *Microelectron. Eng.* **2009**, *86*, 691.
- [26] C. Huang, M. Moosmann, J. Jin, T. Heiler, S. Walheim, T. Schimmel, *Beilstein J. Nanotechnol.* **2012**, *3*, 620.
- [27] R. H. Siddique, Y. J. Donie, G. Gomard, S. Yalamanchili, T. Merdzhanova, U. Lemmer, H. Hölscher, *Sci. Adv.* **2017**, *3*, e1700232.
- [28] Y. J. Donie, D. Theobald, S. Moghadamzadeh, A. Mertens, I. M. Hossain, U. W. Paetzold, U. Lemmer, G. Gomard, *Adv. Opt. Mater.* **2020**, 2001610.
- [29] Y. J. Donie, S. Schliske, R. H. Siddique, A. Mertens, V. Narasimhan, F. Schackmar, M. Pietsch, I. M. Hossain, G. Hernandez-Sosa, U. Lemmer, G. Gomard, *ACS Nano* **2021**, *15*, 7305.
- [30] X. Guo, L. Liu, Z. Zhuang, X. Chen, M. Ni, Y. Li, Y. Cui, P. Zhan, C. Yuan, H. Ge, Z. Wang, Y. Chen, *Sci. Rep.* **2015**, *5*, 15947.
- [31] D. R. Barbero, M. S. Saifullah, P. Hoffmann, H. J. Mathieu, D. Anderson, G. A. Jones, M. E. Welland, U. Steiner, *Adv. Funct. Mater.* **2007**, *17*, 2419.
- [32] A. Klukowska, A. Kolander, I. Bergmair, M. Mühlberger, H. Leichtfried, F. Reuther, G. Grützner, R. Schöftner, *Microelectron. Eng.* **2009**, *86*, 697.
- [33] R. D. Nagel, T. Haeberle, M. Schmidt, P. Lugli, G. Scarpa, *Nanoscale Res. Lett.* **2016**, *11*, 143.
- [34] C. Sanchez, B. Julián, P. Belleville, M. Popall, *J. Mater. Chem.* **2005**, *15*, 3559.
- [35] A. S. Abyzov, J. W. Schmelzer, *J. Chem. Phys.* **2007**, *127*, 114504.
- [36] E. Favvas, A. C. Mitropoulos, *J. Eng. Sci. Technol. Rev.* **2008**, *1*, 25.
- [37] Micro Resist Technology, Processing guidelines-OrmoAtamp, <https://wiki.nanotech.ucsb.edu> (accessed: October 2021).
- [38] E. Y. Arashiro, N. R. Demarquette, *Mater. Res.* **1999**, *2*, 23.
- [39] C. M. Hansen, *Hansen Solubility Parameters: A User's Handbook*, CRC Press, Boca Raton, FL **2007**.
- [40] S. Rasappa, L. Schulte, D. Borah, H. Hulkkonen, S. Ndoni, T. Salminen, R. Sentharamaikanan, M. A. Morris, T. Niemi, *Microelectron. Eng.* **2018**, *192*, 1.
- [41] J. Chen, H. Zhuang, J. Zhao, J. A. Gardella Jr., *Surf. Interface Anal.* **2001**, *31*, 713.
- [42] C. Reichardt, T. Welton, *Solvents and Solvent Effects in Organic Chemistry*, Wiley, New York **2010**.
- [43] Y. Li, K. Hu, X. Han, Q. Yang, Y. Xiong, Y. Bai, X. Guo, Y. Cui, C. Yuan, H. Ge, Y. Chen, *Langmuir* **2016**, *32*, 3670.
- [44] Y. Li, Y. Hao, C. Huang, X. Chen, X. Chen, Y. Cui, C. Yuan, K. Qiu, H. Ge, Y. Chen, *ACS Appl. Mater. Interfaces* **2017**, *9*, 13685.
- [45] C. Lawrence, *Phys. Fluids* **1988**, *31*, 2786.
- [46] A. Budkowski, A. Bernasik, P. Cyganik, J. Raczkowska, B. Penc, B. Bergues, K. Kowalski, J. Rysz, J. Janik, *Macromolecules* **2003**, *36*, 4060.
- [47] L. RunMing, Y. Wei, Z. ChiXing, *Polym. Bull.* **2007**, *59*, 545.
- [48] L. Utracki, *J. Rheol.* **1991**, *35*, 1615.
- [49] S. Wu, F. Zuber, K. Maniura-Weber, J. Brugger, Q. Ren, *J. Nanobiotechnol.* **2018**, *16*, 20.
- [50] Y. J. Donie, M. Smeets, A. Egel, F. Lentz, J. B. Preinfalk, A. Mertens, V. Smirnov, U. Lemmer, K. Bittkau, G. Gomard, *Nanoscale* **2018**, *10*, 6651.
- [51] B. Jiao, Y. Yu, Y. Dai, X. Hou, Z. Wu, *Opt. Express* **2015**, *23*, 4055.
- [52] R. Schmager, I. Hossain, F. Schackmar, B. Richards, G. Gomard, U. Paetzold, *Sol. Energy Mater. Sol. Cells* **2019**, *201*, 110080.
- [53] S. H. Ahn, L. J. Guo, *ACS Nano* **2009**, *3*, 2304.
- [54] M. W. Thesen, D. Nees, S. Ruttloff, M. Rumler, M. Rommel, F. Schlachter, S. Grützner, M. Vogler, A. Schleunitz, G. Grützner, *J. Micro/Nanolithogr., MEMS, MOEMS* **2014**, *13*, 043003.
- [55] J. S. Madsen, M. Geisler, M. B. Lotz, M. Zalkovskij, B. Bilenberg, R. Korhonen, P. Peltonen, P. E. Hansen, S. A. Jensen, *Opt. Express* **2021**, *29*, 3882.
- [56] M. Herder, J. J. Klein, M. Vogler, M.-M. Russew, A. Schleunitz, G. Grützner, in *3D Printing of Optical Components*, (Ed: A. Heinrich), Springer, Cham **2021**, pp. 263–297.
- [57] K. Vynck, M. Buresi, F. Riboli, D. S. Wiersma, *Nat. Mater.* **2012**, *11*, 1017.
- [58] C. Lee, K.-H. Han, K.-H. Kim, J.-J. Kim, *Opt. Express* **2016**, *24*, A488.
- [59] A. Salehi, X. Fu, D.-H. Shin, F. So, *Adv. Funct. Mater.* **2019**, *29*, 1808803.
- [60] S. V. Makarov, V. Milichko, E. V. Ushakova, M. Omelyanovich, A. Cerdan Pasaran, R. Haroldson, B. Balachandran, H. Wang, W. Hu, Y. S. Kivshar, A. A. Zakhidov, *ACS Photonics* **2017**, *4*, 728.
- [61] J. Mao, W. E. Sha, H. Zhang, X. Ren, J. Zhuang, V. A. Roy, K. S. Wong, W. C. Choy, *Adv. Funct. Mater.* **2017**, *27*, 1606525.
- [62] H. Wang, R. Haroldson, B. Balachandran, A. Zakhidov, S. Sohal, J. Y. Chan, A. Zakhidov, W. Hu, *ACS Nano* **2016**, *10*, 10921.
- [63] N. Pourdavoud, S. Wang, A. Mayer, T. Hu, Y. Chen, A. Marianovich, W. Kowalsky, R. Heiderhoff, H.-C. Scheer, T. Riedl, *Adv. Mater.* **2017**, *29*, 1605003.
- [64] B. Dou, J. B. Whitaker, K. Bruening, D. T. Moore, L. M. Wheeler, J. Ryter, N. J. Breslin, J. J. Berry, S. M. Garner, F. S. Barnes, S. E. Shaheen, C. J. Tassone, K. Zhu, M. F. A. M. V. Hest, *ACS Energy Lett.* **2018**, *3*, 2558.
- [65] R. Schmager, G. Gomard, B. S. Richards, U. W. Paetzold, *Sol. Energy Mater. Sol. Cells* **2019**, *192*, 65.
- [66] I. M. Hossain, D. Hudry, F. Mathies, T. Abzieher, S. Moghadamzadeh, D. Rueda-Delgado, F. Schackmar, M. Bruns, R. Andriessen, T. Aernouts, F. D. Giacomo, U. Lemmer, B. S. Richards, U. W. Paetzold, A. Hadipour, *ACS Appl. Energy Mater.* **2018**, *2*, 47.
- [67] M. Worgull, *Hot Embossing: Theory and Technology of Microreplication*, William Andrew **2009**.
- [68] J. Crocker, E. Weeks, What is the pair correlation function, <http://physics.emory.edu> (accessed: October 2021)
- [69] M. D. Abràmoff, P. J. Magalhães, S. J. Ram, *Biophotonics Int.* **2004**, *11*, 36.
- [70] D. Nečas, P. Klapetek, *Open Phys.* **2012**, *10*, 181.